Photoacoustics 3 (2015) 3–10

Contents lists available at ScienceDirect

Photoacoustics

journal homepage: www.elsevier.com/locate/pacs

Sono-photoacoustic imaging of gold nanoemulsions: Part I. Exposure thresholds

Bastien Arnal [a,*], Camilo Perez [a,c], Chen-Wei Wei [a], Jinjun Xia [a], Michael Lombardo [a,b], Ivan Pelivanov [a,d], Thomas J. Matula [a,c], Lilo D. Pozzo [a,b], Matthew O'Donnell [a]

[a] University of Washington, Department of Bioengineering, 616 NE Northlake Place, Seattle, WA 98105, United States
[b] University of Washington, Department of Chemical Engineering, Box 351750, Seattle, WA 98195-1750, United States
[c] Center for Industrial and Medical Ultrasound, Applied Physics Laboratory, University of Washington, 1013 NE 40th Street, Seattle, WA 98105-6698, United States
[d] International Laser Center, Moscow State University, Moscow, Russian Federation

ARTICLE INFO

Article history:
Received 25 August 2014
Received in revised form 19 November 2014
Accepted 11 December 2014

Keywords:
Photoacoustic cavitation
Vaporization
Gold nanoparticles
Nanoemulsion
Perfluorocarbon
Non-linear photoacoustics

ABSTRACT

Integrating high contrast bubbles from ultrasound imaging with plasmonic absorbers from photoacoustic imaging is investigated. Nanoemulsion beads coated with gold nanopsheres (NEB-GNS) are excited with simultaneous light (transient heat at the GNS's) and ultrasound (rarefactional pressure) resulting in a phase transition achievable under different scenarios, enhancing laser-induced acoustic signals and enabling specific detection of nanoprobes at lower concentration. An automated platform allowed dual parameter scans of both pressure and laser fluence while recording broadband acoustic signals. Two types of NEB-GNS and individual GNS were investigated and showed the great potential of this technique to enhance photoacoustic/acoustic signals. The NEB-GNS size distribution influences vaporization thresholds which can be reached at both permissible ultrasound and light exposures at deep penetration and at low concentrations of targets. This technique, called sono-photoacoustics, has great potential for targeted molecular imaging and therapy using compact nanoprobes with potentially high-penetrability into tissue.

1. Introduction

Contrast-enhanced imaging with exogenous contrast agents is a rapidly developing technique for both photoacoustic (PA) and ultrasound (US) systems. Microbubbles have been used in US harmonic imaging [1] of vasculature, and for drug delivery [2] or cavitation-based treatments [3]. Their large size (typically 1–10 μm), however, inhibits high penetrability into tissue through leaky vasculature (300–500 nm endothelial gaps) and nanoscale pores, and through active mechanisms such as cellular uptake. Making stable nanobubbles at the dimensions required for enhanced transport is currently a challenge [4].

To solve this problem, phase-change contrast agents, which change state from liquid to gas if exposed to thermal and/or acoustic energy, were introduced. Liquid perfluorocarbon nanodroplets with a low-boiling point and a physical dimension appropriate for enhanced penetrability into tissue have been developed [5–8]. The phase-transition of these nanodroplets into a microbubble (vaporization) produces high contrast for US imaging. Compared to other US contrast agents, nanoemulsions can have a long circulation in the body (up to 2 h [8]). Because of increased surface tension, however, US exposure parameters must be relatively high, usually involving high repetition rates [7] or long excitations (~100 ms) [6]. This means that heat can be involved in the vaporization, increasing the possibility to damage surrounding tissues or limiting the repetition rate of the imaging modality. This mechanism is also not efficient using low-frequency ultrasound because of low acoustic absorption.

To achieve molecular imaging at significant depths within tissue, nanoscale, laser-activated PA contrast agents have been introduced [9–13]. Plasmonic absorption enhances the efficiency of compact nanoprobes (10–200 nm) in PA generation. However, a significant concentration is usually required to get single shot measurements for real-time *in vivo* imaging (*e.g.* ~10 nM) [9–13]. Recent studies have shown that combining nanodroplets with efficient optical absorbers in a single contrast agent can enhance the PA signal from the absorbers [12]. Here we build on this work to demonstrate a highly sensitive, and potentially specific, approach for molecular imaging and therapy using a nanoscale contrast agent integrating

* Corresponding author. Tel.: +1 80 96 33 45
E-mail address: bastien.arnal@gmail.com (B. Arnal).

http://dx.doi.org/10.1016/j.pacs.2014.12.001

perfluorocarbon nanodroplets with plasmonic absorbers. In particular, we explore the non-linear acoustic response of these agents to simultaneous light and sound excitations at exposure levels well within safety limits for routine diagnostic imaging.

In our previous work, we introduced a nanoemulsion of perfluorohexane droplets (100–200 nm) surrounded by amphiphilic gold nanopsheres (12 nm in diameter). It was used as a non-linear PA contrast agent by inducing a phase transition of the oil through plasmonic absorption of light by the gold nanoparticles [14]. This approach can produce highly sensitive PA images with high background suppression (*i.e.*, also highly specific contrast), but it requires a relatively high optical fluence to observe non-linear contrast (at 750 nm, threshold at 4 mJ/cm^2, 10 dB contrast around 6 mJ/cm^2), limiting its use for deep imaging applications.

An approach to greatly reduce the optical fluence required for a non-linear response from these contrast agents is suggested by recent work showing that laser generation of water vapor bubbles around plasmonic absorbers can be enhanced by adding ultrasound pressure fields [15–17]. This technique, named "PA cavitation", enables high contrast imaging at lower exposure thresholds and concentrations. Building on this work, we investigate here the PA cavitation exposure thresholds needed to trigger vaporization of a nanoemulsion bead coated with gold nanopsheres (NEB-GNS). This approach leverages short-lived (a few μs) bubbles made possible by the high boiling point (BP) of the perflurocarbon used in this nanoemulsion. In contrast to another approach using long lifetime bubbles [12], a short-lifetime strategy using reversible phase transitions is preferred for molecular imaging applications requiring extended exposures. Using PA cavitation, the detection sensitivity for imaging can be enhanced by two physical effects: higher thermal expansion will enhance the PA response and the emitted ultrasound field will instantly scatter on the generated bubbles.

In the remainder of this paper, we investigate the benefit of clustering small gold nanopsheres around high-BP perfluorocarbon droplets for combined PA/US applications. After introducing the physical characteristics of the NEB-GNS agent, vaporization thresholds are quantified and compared to single gold nanopsheres. The potential use of the vaporization signals for imaging is then studied and discussed. To specifically retrieve the vaporization signal in tissues loaded with NEB-GNS, photoacoustic and backscattered ultrasound signals must be canceled by a procedure described in a future publication called "sono-photoacoustic" imaging.

2. Materials and methods

2.1. Nanoemulsion samples

NEB-GNSs were synthetized using the procedure described in previous reports [18,19]. Colloidal GNSs (diameter 12 nm) were synthetized using a citrate reduction method [20]. The particles were functionalized using PEG-thiol and butane-thiol (Sigma–Aldrich, St. Louis, MO, USA), with dosages of 0.8 chains/nm^2 Au and 700 molecules/nm^2 Au respectively. Attraction between the hydrophobic butane-thiol ligands resulted in clustered GNS dispersions. A solution of 1 vol% perfluorohexane (Sigma–Aldrich, St. Louis, MO, USA) and 0.012 vol% Au clusters in water was sonicated (102C, Branson, Danbury, CT, USA, pulsed regime – 1 s on, 4 s off) for 13 s in a cold water bath.

The absorbance was measured with a spectrophotometer (UV 1601, Shimatzu, Kyoto, Japan). The absorbance spectrum (cf Fig. 1a, blue curve) exhibits a red shift of the resonance from 520 nm to 547 nm compared to the original gold nanopsheres (black curve) and a broad tail enhancing absorption in the optical window ([600–1100] nm wavelengths). The size was measured by DLS as a broad dispersion between 30 nm and 1.2 μm with a peak at 132.1 nm and a mean size of 303 nm (cf Fig. 1b). Additional complexes were identified between 2 and 6 μm, but DLS may not be quantitative in this range as it is heavily affected by sedimentation or flotation [21]. In our case, the effective density of perfluorohexane beads (1.7 g/cm^3) can be increased by the GNS (density 19.3) resulting in sedimentation speeds depending on size.

To confirm the presence and quantify the micron-size particle number, the size distribution and concentration of the emulsion were obtained prior to and after all experiments using a Coulter Multisizer III (Beckman Coulter, Miami, FL). A 20 μm aperture was used, which can size particles with diameters from 0.56 to 12 μm and considers any count below 0.56 μm as the noise level. The sample was diluted ∼1250× on a 0.2 μm filtered ISOTON II electrolyte (Beckman Coulter, Miami, FL). A 50 μL sample was used each time, and all measurements were repeated 6 times using a volumetric count mode. Individual particles were sized and binned in 300 evenly spaced bins with 0.039 μm width. All data are reported as a histogram with count *vs.* diameter, with the count (bin height) showing the number of particles in each bin interval. The reported concentration is computed for all ranges in question and accounts for the dilution factor and sampling volume used above.

A near Gaussian distribution of NEB-GNS was identified between 1 and 3 μm (cf inset of Fig. 1b). The sample was then split in two volumes. Assuming an ideal covering of the bead by gold nanopsheres (80% surface density), the weight of each bead size was calculated. Then, a basic model of sedimentation (Stokes force = gravity) was used to calculate the sedimentation speeds of different particles: *e.g.*, in 24 h a 425 nm particle sinks 22 mm. In contrast, a 132 nm bead should sink only 6 mm in the same period. A sample of 10 ml was left to settle in a scintillation vial. As 22 mm was the height of our solution in the vial, we assume that all

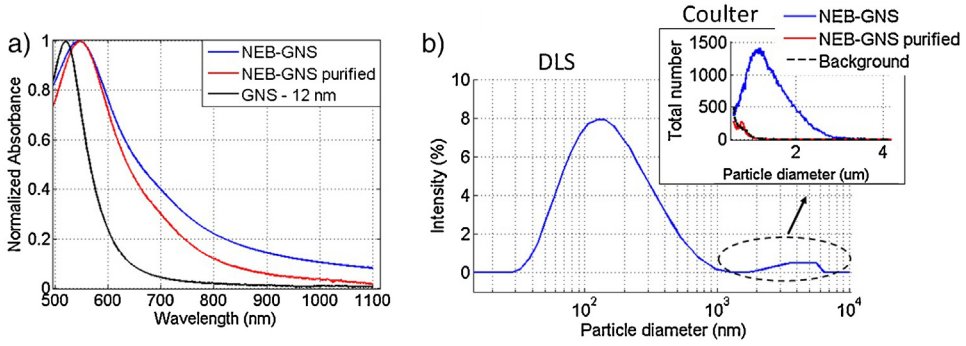

Fig. 1. (a) Absorbance spectra of the nanoemulsion before (blue) and after purification (red), and of gold nanopsheres in suspension (black). (b) Sizing of the nanoemulsion by DLS (intensity). Inset: Sizing in the micron range using a Coulter counter: nanoemulsion before (blue) and after purification (red); background signal is shown in black.

particles larger than 425 nm will fall to the bottom. An 8 ml sample was carefully withdrawn from the top without provoking any agitation. This supernatant was sized again with the Coulter counter. There were no particles larger than 1 micron (inset Fig. 1b), which validated the purification process. These samples were used to compare the vaporization threshold before and after purification. The purified NEB-GNS sample showed a less broad tail than the original one (cf Fig. 1a), indicating that larger beads tend to broaden the extinction spectrum.

We performed Discrete Dipole Approximation (DDA) simulations using DDscat [22] to estimate the contributions of scattering and absorption on NEB-GNS. An oil bead of 150 nm diameter was surrounded by 12 nm GNS positioned using an optimization code solving the Thomson problem leaving a gap of 2 nm between spheres. The NEB-GNS structure was discretized using a step of 1.35 nm and the simulation was run with orientational averages. The broadening of the tail was observed for both absorption and scattering contributions, but scattering contributes to less than 20% of the extinction and is not particularly higher at the longer wavelength. Hence, it is likely that absorption dominates over scattering, at least for the purified sample, meaning NEB-GNS absorption can be related to the absorbance measurement.

2.2. Sample preparation

Using a size-dependent concentration measurement from DLS, we estimate the concentration of emulsion bead in the stock solution to be 1.32×10^{12} beads/ml (for sizes ranging from 100 to 8000 nm), or about 2.2 nM. For all experiments, the solution was diluted to a fixed absorbance of 0.25 cm^{-1} at 750 nm, leading to a concentration of 3.8×10^{10} beads/ml (or 63 pM) for the raw sample and 5.86×10^{10} beads/ml (or 94 pM) for the purified sample (lower tail after filtration, cf Fig. 1b).

A sample of GNS obtained after a citrate reduction method was diluted with citrate buffer (3.8 mM) to obtain an absorbance matching the NEB-GNS one at 520 nm (0.403 cm^{-1}). The concentration of GNS was then 2.59×10^{12} GNS/ml. The concentrations of GNS and NEB-GNS samples were estimated respectively to be 3.8×10^{12} GNS/ml and 5.9×10^{12} GNS/ml, *i.e.*, on the same order.

2.3. Ultrasound transducer calibration

The pressure field generated by a focused ultrasound transducer (H-102, Sonic Concept, Woodinville, WA, USA, focused at 63 mm, f# 0.98, 1.24 MHz) in line with a 55 dB gain power amplifier (ENI-A150) was quantified using a fiber optic hydrophone (FOPH 2000, Aperture 100 μm, RPI Acoustics, Germany). This hydrophone is calibrated at lower frequencies (down to 100 kHz) and provides a broadband (up to 100 MHz) frequency response for accurate non-linear acoustic measurements. The HIFU transducer, mounted at one end of a degassed and deionized water bath, was driven by a 10 cycle sine-burst produced by a function generator (33120A, Agilent, Palo Alto, CA) together with the power amplifier and a customized matching network. A 10 MΩ high voltage probe (Teledyne LeCroy, Chestnut Ridge, NY) was inserted between the matching network and the power amplifier to measure the input voltage applied to the driving system. A 3D positioning system was used to move the fiber optic probe hydrophone at the focus. Hydrophone signals were digitized by an oscilloscope (LT344 Waverunner, LeCroy, NY) at 500 MSample/s. The FOPH 2000 software CALDEC was used to calculate the pressure from oscilloscope data and to deconvolve the signal to account for the frequency response of the system [23]. As minimal thermal effects result from ultrasound with a 10-cycle pulse at low repetition rate (5 Hz), peak negative (p−) pressure alone is reported and corresponds to the minimum pressure measured in the pulse.

2.4. Automated setup for light and sound exposure threshold study

A 532-nm pump beam was injected into a wavelength-tunable optical parametric oscillator (OPO) cavity (Surelite OPO plus, Continuum, Santa Clara, CA, USA) to produce 10-ns duration, 750-nm laser pulses. Before coupling the laser beam into a fiber bundle (77526, Oriel Instruments, Stratford, CT, USA) for delivery to the sample, the fluence was adjusted with a combination of neutral density filters that can be remotely switched with a six-position filter wheel (FW-103, Thorlabs, NJ, USA), as shown on the top left of Fig. 2a. The sample (diluted NEB-GNS solution or GNS) was injected into a customized transfer pipet (3 ml, BD Falcon, NJ, USA) connected to a tube in a closed loop. The tubing was coupled to a peristaltic pump (Masterflex L/S model 7518-60, Cole-Parmer, IL, USA), allowing circulation of the sample between each dataset. The pump likely induced static pressure changes and was not used during acquisitions. On the edge of the transfer pipet facing the focused ultrasound transducer (H-102, Sonic Concept, Woodinville, WA, USA, focused at 63 mm, f# 0.98, 1.24 MHz), a black marker spot of 1 mm diameter was drawn for alignment purposes.

The sample was immersed into ultra-pure degassed water and was roughly positioned at the focus of the transducer by maximizing the pulse-echo signal received on the focused transducer. Then, the laser was fired at a low fluence on the black marker spot and the PA signal was maximized on the focused transducer, allowing more precise positioning. An in-house PVDF unfocused sensor (bandwidth [0.05–30 MHz], aperture 6 mm diameter) was then positioned at the water surface 70 mm from the sample. The timing of ultrasound emissions and laser firing was adjusted. The PVDF first received the PA signal from the black

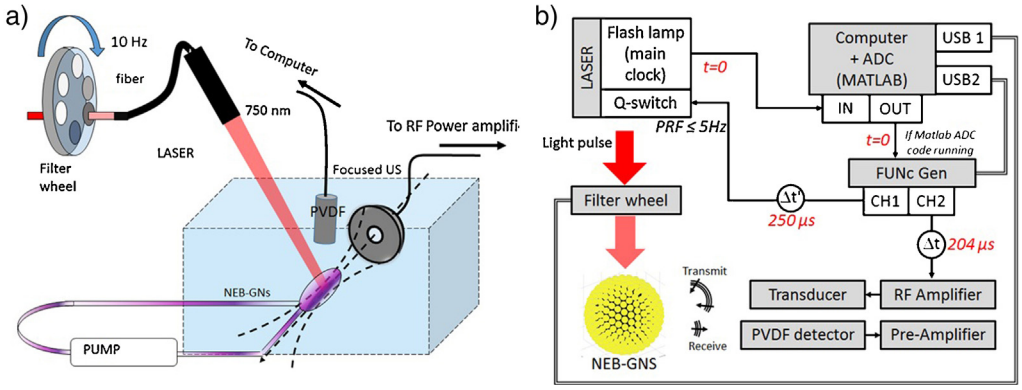

Fig. 2. Setup for automated parameter scan of laser fluence and acoustic pressure. (a) Light and sound delivery and sample position. (b) Instrumentation with remote controls. The reader should follow the diagram starting from the flash lamp signal ($t = 0$).

marker spot when only the laser was fired. Then, US pulses were emitted and the echoes generated on the edge of the pipet were measured with the PVDF transducer. By changing the trigger delay controlling the duration between the acoustic emission and the lasing time, the arrival time of the PA signal was matched to the one of the 5th acoustic cycle, meaning the laser is fired on the sample when the 5th US cycle reaches it. Note, that the laser beam size of 6 mm is larger than the acoustic wavelength (1.2 mm) and covers multiple peak negative pressure sites. Thus, contrary to our preliminary experiment where the light was focused on a 1 mm area [28], the exact lasing time in the microsecond range will not affect the results. Broad illumination is also more representative of potential *in vivo* applications. The sample was then moved horizontally toward the transducer, allowing both the focal spot of the transducer and the laser spot to meet within the pipet bulb. As noted above, a 10-cycle ultrasound pulse emitted with the focused US transducer was used for all studies. The laser was fired at the arrival time of the 5th acoustic cycle at the transducer focus.

To cover all desired exposure ranges in terms of laser fluence and US pressure while recording enough data to perform statistics, an automated platform was designed. A TTL signal running at 20 Hz, corresponding to the flash lamp timing of the laser, is used as an input trigger to an ADC board (Razor 14X2 Express CompuScope, Gage, Lockport, IL, USA) controlled with Matlab. When the software is running, a trigger out is sent by the ADC board immediately after being triggered. This signal is then delayed by 250 μs by a function generator (AFG-3252, Tektronix, OR, USA) to trigger the laser Q-switch. This approach limits exposure of the samples since lasing only occurs when a signal is actually being recorded. Moreover, the repetition rate was limited to 5 Hz by the Matlab software. The second channel of the generator was used to drive an RF amplifier (A150, ENI, USA) at a voltage also controlled by software to independently scan the pressure amplitude. Ultrasound was emitted earlier than the laser so that it could propagate to the region under study. The PVDF transducer finally received both the laser-induced PA signals and the scattered pressure waves originating from the focused transducer. This RF signal was captured by the ADC, displayed in real-time and saved on the computer hard-drive for further analysis. At each set of exposure parameters, 200 recordings were performed. The laser fluence was gradually increased. For each laser fluence, the ultrasound pressure was raised until significant cavitation activity was noted.

Fluence values were calibrated by placing an energy meter (J-power, Coherent, Santa Clara, CA) at a position matching the focus of the US transducer. A 2-mm pinhole was used, ensuring that it was at the maximum energy position of the laser beam. Then, light attenuation through 60-mm of water was taken into account to report all fluence values.

2.5. Data analysis

For each set of exposure parameters, a reference signal recorded without laser firing was subtracted from the 200 signals to remove the US scattered wave contributions from the plastic container, similar to methods used in our previous studies [28]. This subtraction was robust and produced residual signals outside the time window of interest much smaller than those obtained during laser excitation studies. The broadband noise signal was computed in a time window before the lasing time. If no bubble is present, the differential signal should correspond to pure noise. In contrast, the presence of vapor will automatically generate some scattered acoustic signals in all directions. To detect the vaporization events, a threshold on the magnitude of the signals equal to 2 times the noise value was chosen to count the number of cavitation events out of the 200 independent recordings. This threshold was set arbitrarily and the results were not highly influenced by its value, indicating that our detection method is very sensitive. A sigmoidal function was fit to all broadband noise dependencies at each laser fluence to compute the cavitation threshold, defined as the peak negative acoustic pressure corresponding to a 50% probability of a cavitation event.

3. Results

3.1. Cavitation signals

After removing the contribution from the tube using a reference signal, the recorded signals clearly exhibited the presence of cavitation. With the same exposure parameters, a small cavitation event can be distinguished in Fig. 3b from no cavitation in Fig. 3a. Cavitation always occurred at the lasing time depicted by the red dotted line. A larger cavitation event is shown in Fig. 3c with 10-fold amplitude compared to the small cavitation (note scale change). Normalized spectra for both of these signals are shown in Fig. 3d. The broadband noise characteristics are present in both signals, although the main harmonic is relatively higher for the large cavitation event.

3.2. Vaporization probabilities

The resulting cavitation probabilities as a function of US peak negative pressure are shown for the NEB-GNS and purified NEB-GNS samples in Fig. 4a and b. For both samples, cavitation activity was not consistently observed using the 10-cycle ultrasound pulse alone, even at pressures exceeding 8 MPa (below 20% for the raw sample and 2% for the purified one; results are not shown). In contrast, a small fluence (0.64 mJ/cm^2) already creates consistent vaporization at 1.5 MPa for the raw sample and at 2.5 MPa for the purified one. Higher fluences decrease the vaporization threshold. Note that for the purified sample, and at such a low concentration,

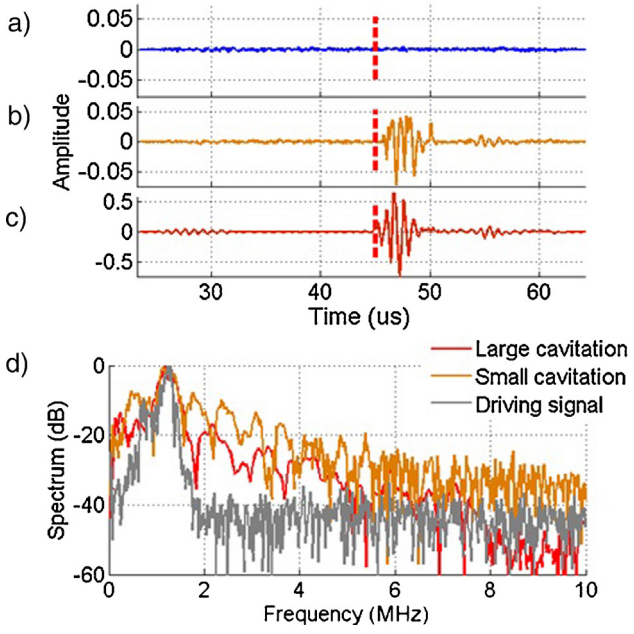

Fig. 3. Wideband detection of cavitation events using a PVDF detector. Lasing time is shown with the red dotted line and the ultrasound 10-cycle pulse travels to the focus starting from the blue dotted line time. (a)–(c) Signals after differentiation. (a) and (b) No cavitation and cavitation (probability 5%) with exposures of F_0 = 0.641 mJ/cm^2, p− = 1.74 MPa. (c) Large cavitation (F_0 = 4.7 mJ/cm^2, p− = 1.43 MPa). (d) Normalized spectra of differential signals for large (red), small (orange) and spectrum of the driving signal at 1.24 MHz.

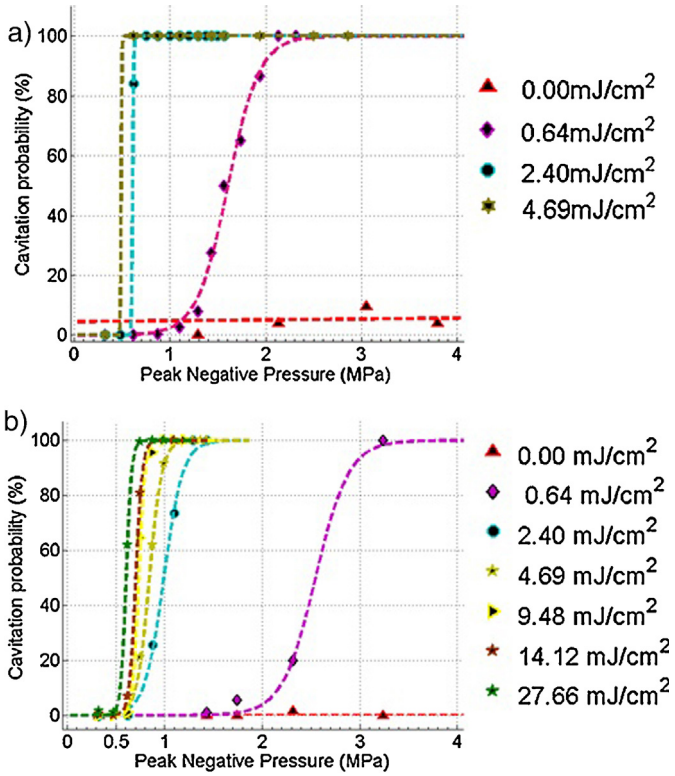

Fig. 4. Photoacoustic cavitation probabilities of emulsion sample #1 before (a) & after purification (b).

a very high laser fluence of 27.7 mJ/cm^2 is only efficient for vaporization at 0.6 MPa, and that raising the fluence from 9.48 to 27.7 mJ/cm^2 doesn't change the cavitation threshold dramatically.

These results show that combining light (transient heating) and short ultrasound pulse (pressure) exposures is much more efficient than using each of them separately.

3.3. Summary of the vaporization results and comparison with a GNS sample

A summary of the vaporization threshold (50% probability) of the GNS-NEB samples (raw and purified) and the GNS 12 nm sample is presented in Fig. 5. For a peak negative pressure of 1.0 MPa, the fluence threshold of the GNS is reduced by a factor of 12 for the raw sample and by a factor of 6 for the filtered sample.

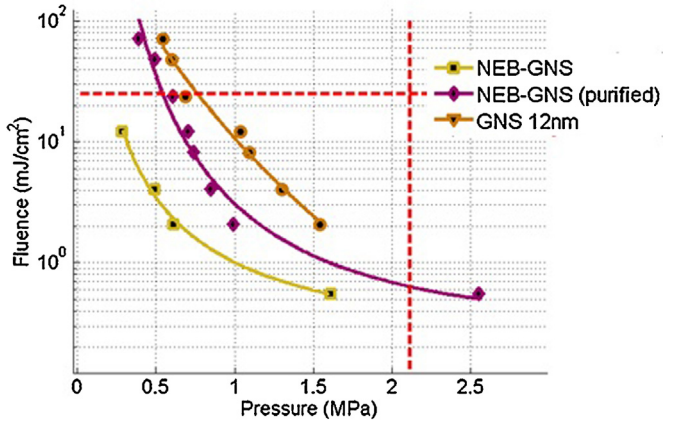

Fig. 5. Summary of vaporization thresholds. Each point in the Fluence/Peak negative pressure plane corresponds to a 50% vaporization probability. NEB-GNS, NEB-GNS purified and GNS. The red dotted lines indicate: the mechanical index (MI) FDA limitation of 1.9 for ultrasound imaging (vertical) and the permissible optical fluence exposure of 25 mJ/cm^2 (horizontal).

3.4. Sono-photoacoustic signal enhancement

For imaging purposes, the amplitude emitted by the bubbles will determine detection sensitivity. In addition, the non-linear nature of sono-photoacoustic signal enhancement may lead to a highly specific agent. To explore this hypothesis, the signals presenting cavitation within each data set were isolated. Then, the median value and the standard deviation of the maximum amplitude in time of these signals were calculated.

In Fig. 6, the sono-photoacoustic signal clearly evolves in a non-linear manner as a function of acoustic peak negative pressure for both the raw sample and the purified one. Note that amplitudes are higher in Fig. 6a than in Fig. 6b. The bubble signatures had in fact similar amplitudes at a fixed pressure. The error bars denote the standard deviation σ of the amplitudes within the ensemble of cavitation events with a length equal to 2σ. While the cavitation threshold decreases with laser fluence, the amplitude of cavitation events does not change with pressure when the fluence is above a threshold (above 2.4 mJ/cm^2 for both samples). This result suggests the potential for deep sono-photoacoustic imaging.

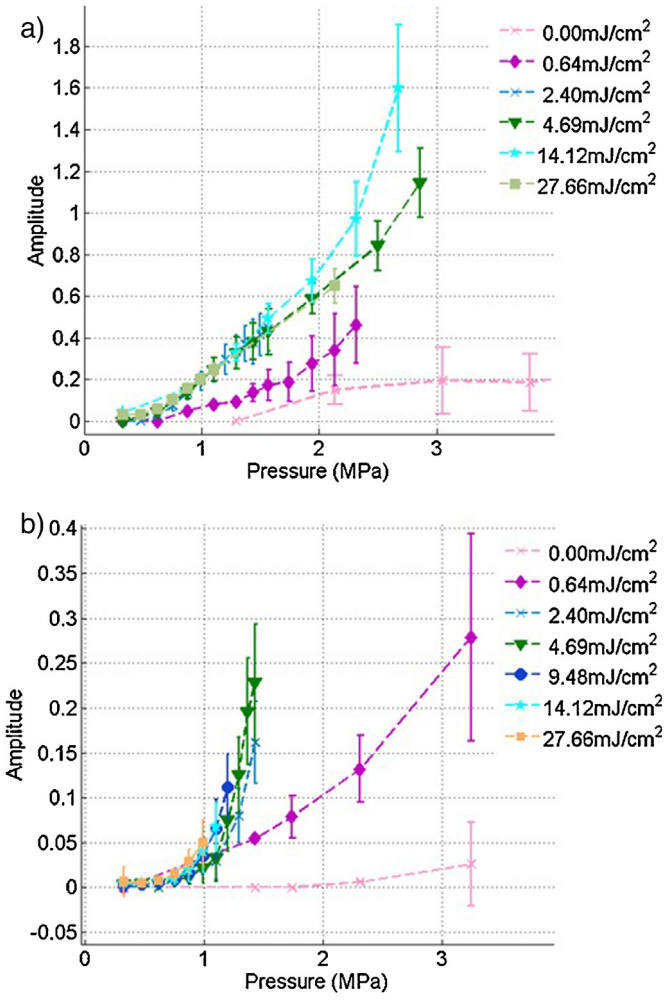

Fig. 6. Amplitude of sono-photoacoustic signals as a function of acoustic pressure at different fluences. (a) NEB-GNS sample. (b) NEB-GNS purified sample.

4. Discussion

In this paper, we have demonstrated the potential of a novel contrast agent composed of nanoemulsion beads surrounded by gold nanospheres using simultaneous light and sound excitation. A robust emulsion characterization platform, which performs a 2-dimensional parameter scan (pressure and light) for cavitation threshold determination, was developed and introduced. This platform will be particularly beneficial for future testing and comparison of new nanoemulsion contrast agent formulations.

The exposure parameters required to achieve PA cavitation were extensively studied at a picomolar concentration of contrast agent ($2–6 \times 10^{10}$ beads/ml). Ultrasound pressures were varied from 0.1 MPa to 9 MPa at focal peak negative pressures and laser fluences varied from 0.4 to 27.6 mJ/cm^2. As laser fluence increased, the cavitation threshold (in terms of US peak negative pressure) decreased to values far below the FDA mechanical index (MI < 1.9) limitation.

From Fig. 4, it is clear that the cavitation probability for ultrasound exposure alone remained low for pressures up to 4 MPa (<10%). The pressure for ultrasound exposure alone was scanned up to 9 MPa (not shown in Fig. 4) yet we did not reach a 50% probability of cavitation (dashed pink line). Previous work with similar nanoemulsions, in terms of boiling points and sizes, explored acoustic droplet vaporization thresholds of dodecafluoropentane (DDFP, boiling point in bulk = 29 °C) and of 2H,3H-perfluoropentane (H-PFP, boiling point in bulk = 55 °C) albumin-coated droplets with a mean diameter of approximately 260 nm, and 630 nm, respectively [24]. These nanoemulsions were included in albumin-acrylamide gel phantoms and sonicated with 10 cycle HIFU pulses (f = 2 MHz, pulse repetition = 5 s), similar to our setup (1.24 MHz). For DDFP, an ultrasound peak negative pressure threshold was found at 8.50 MPa. In the case of H-PFP, the pressure was increased up to 8.7 MPa without evidence of vaporization. Our results are consistent with this study [24]. When exposed to 5 MHz, micron-scale perfluoropentane droplets vaporization thresholds decreases with droplet diameter [25] as surface tension decreases. As the purification process removes particles larger than 600 nm, the observed increase of vaporization threshold is consistent with previous studies. Additionally, many studies reported a decreasing vaporization pressure as a function of increasing US frequency [26,27]. As mentioned earlier, heat seems to be necessary to overcome surface tension stabilization. Our study shows that this heat can be delivered in a controlled and targeted way by plasmonic light absorption. Further work could study photoacoustic vaporization thresholds of NEB-GNS at higher frequencies to find the optimal configuration to implement real-time sono-photoacoustic imaging.

Preliminary imaging experiments (not shown here) suggest that particles accumulated at the bottom of the sample. Single nanoparticles are mostly subject to diffusion and gravity can usually be neglected. In contrast, gravity effects can be dominant for large oil droplets (1.7 density) and is amplified by the gold particles on the surface. We took advantage of these effects to purify our sample. A centrifugation technique could have been used, but it was not preferred because it could increase the probability of aggregation of beads at the bottom of the container. Similarly, extrusion through membrane filters could lead to more consistent size distributions, but it could also generate new distributions of beads since extrusion can actually help create droplets. It could also result in the loss of products trapped on the membrane surface.

Further work could investigate the best way to purify NEB-GNS samples. DLS measurements have to be complemented with other sizing techniques such as a Coulter counter to quantify the amount of micron-scale beads if high penetrability is needed (*i.e.* particles >500 nm will not penetrate the gaps in leaky vasculature). Even a very small amount of larger beads can greatly affect the measured vaporization thresholds as their volume is far larger. A strategy using a broad distribution such as our raw sample (100 nm–6 μm) can image vasculature scales from large vessels to capillaries, with the ability to penetrate leaky vasculature only for the smaller particles.

Previous high speed photomicrography studies on the same emulsion type showed the short lifetimes ~1.2 μs for the vapor bubbles under light exposure only [28], suggesting that the perfluorocarbon beads also go back to the liquid state when the ultrasound field vanishes. The fate of the gold nanoparticles during bubble expansion and after condensation has not been studied yet. Nevertheless, additional experiments have also shown a strong consistency in the cavitation activity after several thousand shots, indicating that the gold particles remain somehow coupled to the beads. Observing a single emulsion bead flowing into a small channel and exposed to light and sound could lead to better characterization [29].

Photoacoustic cavitation is surprisingly induced in the GNS sample composed of small particles (15 nm diameter) at a wavelength (750 nm) where optical absorption is very weak. Previous work has only studied photoacoustic cavitation of large diameter GNS (82 nm diameter) at the plasmonic resonance wavelength (532 nm) [17]. Here, the mean distance between GNS is 72 μm given the size and concentration, so coupling effects should not play a role in effective vapor bubble creation unless there is particle aggregation due to acoustic streaming, or other pressure-induced effects. Further modeling inspired by previous work [30,31] could focus on explaining this behavior. Compared to the emulsion beads, the liquid volume to vaporize is not the same and the total energies necessary to achieve vaporization might not be comparable.

As the probability of cavitation increases (see Fig. 6), we have shown that the amplitude of the resultant acoustic signal does not increase with laser fluence for fluences higher than 2.4 mJ/cm^2. This means that when the phase transition occurs, a higher laser fluence does not affect the vaporization signals as much as the US pressure does. The laser pulse induces heat within a short 30–40 ns time window enabling the phase transition. Then, it appears that the bubble size is more influenced by the pressure field, which also controls the amplitude of bubble-generated acoustic waves. As extinction by soft tissue limits light penetration, a scenario of low laser fluence with a maximum permissible pressure would be ideal for contrast enhancement. Depending on the tissue types between the light source and the region of interest, such light penetration can be achieved from one to a few centimeters deep into tissue. A Monte Carlo simulation [31] of light transport was performed through skin (thickness ΔZ = 1.12 mm, absorption coefficient μ_a = 0.49 cm^{-1}, scattering coefficient μ_s = 82.6 cm^{-1}, anisotropy g = 0.75), fat (ΔZ = 2 mm, μ_a = 0.1 cm^{-1}, μ_s = 115 cm^{-1}, g = 0.9) and muscle (ΔZ = 30 mm, μ_a = 0.09 cm^{-1}, μ_s = 216 cm^{-1}, g = 0.9). Using a gaussian beam (width: 2 cm, λ = 750 nm, maximum fluence: 25 mJ/cm^2), fluences of 2 mJ/cm^2 and 0.6 mJ/cm^2 were respectively reached at depths of 1.6 and 2.0 cm. Future studies could explore the penetration limits for different imaging applications.

Finally, thanks to the clustering of gold nanopsheres on an emulsion bead, and to the resulting large signal from the bubble, these measurements succeeded even at low concentration in a regime where single shot linear PA imaging fails (0.25 cm^{-1}). The nanoemulsion structure and synthesis can be further improved to reach higher efficiency, for example using another perfluorocarbon oil with a lower boiling point [25,32]. Future studies will explore the relationship between both threshold and acoustic signal strength as a function of concentration.

Based on this work, a real-time imaging system could achieve sono-photoacoustic imaging of NEB-GNS at depths exceeding several centimeters and at ultra-low concentration levels. This

imaging approach could rely on single cycle or multiple cycles US excitations, depending on the desired imaging range. However, to use this technique for *in vivo* imaging, scattered ultrasound and photoacoustic signals must both be canceled to retrieve the specificity of vaporization signals and perform accurate background suppression. A way to implement sono-photoacoustics in a real-time imaging sequence will be demonstrated in a companion publication. Moreover, inertial cavitation produced by this nanoemulsion already has been exploited for *in vitro* sonothrombolysis [28,33]. Further work can rely on this study to optimize the delivery of this treatment and its monitoring.

5. Conclusion

This work showed the potential of gold-coated nanoemulsion beads excited with simultaneous pulsed laser and ultrasound. A fully automated setup for dual exposure parameter scanning was designed for quantitative assessment of vaporization thresholds of the NEB-GNS. A phase transition of the nanoemulsion bead occurred at much lower peak negative pressure when laser fluence increased. We demonstrated that NEB-GNS vaporization could be achieved at a reduced exposure compared to the vaporization of water surrounding single GNS. The high amplitude of vaporization signals produced by simultaneous pulsed light and ultrasound exposure could be used to design an imaging modality allowing both high specificity and sensitivity of nano-contrast agent detection. The results could also be applied to drug delivery using nanodroplets with high encapsulation energy and to localized or targeted therapies using nanoagents.

Conflict of interest statement

The authors declare that there are no conflicts of interest.

Acknowledgments

This work was supported in part by NIH RO1-EB016034, R01-CA170734, RO1-HL121226, the Life Sciences Discovery Fund 3292512, NSF CBET-1236309, and the Department of Bioengineering at the University of Washington.

References

[1] Wei K, Jayaweera AR, Firoozan S, Linka A, Skyba DM, Kaul S. Quantification of myocardial blood flow with ultrasound-induced destruction of microbubbles administered as a constant venous infusion. Circulation 1998;97:473–83.
[2] Ferrara K, Pollard R, Borden M. Ultrasound microbubble contrast agents: fundamentals and application to gene and drug delivery. Annu Rev Biomed Eng 2007;9:415–47.
[3] Unger EC, Porter T, Culp W, Labell R, Matsunaga T, Zutshi R. Therapeutic applications of lipid-coated microbubbles. Adv Drug Deliv Rev 2004;56:1291–314.
[4] Cavalli R, Bisazza A, Trotta M, Argenziano M, Civra A, Donalisio M, et al. New chitosan nanobubbles for ultrasound-mediated gene delivery: preparation and in vitro characterization. Int J Nanomed 2012;7:3309–18.
[5] Rapoport N, Gao Z, Kennedy A. Multifunctional nanoparticles for combining ultrasonic tumor imaging and targeted chemotherapy. JNCI – J Natl Cancer Inst 2007;99:1095–106.
[6] Giesecke T, Hynynen K. Ultrasound-mediated cavitation thresholds of liquid perfluorocarbon droplets in vitro. Ultrasound Med Biol 2003;29:1359–65.
[7] Kripfgans OD, Fowlkes JB, Miller DL, Eldevik OP, Carson PL. Acoustic droplet vaporization for therapeutic and diagnostic applications. Ultrasound Med Biol 2000;26:1177–89.
[8] Rapoport N, Nam K-H, Gupta R, Gao Z, Mohan P, Payne A, et al. Ultrasound-mediated tumor imaging and nanotherapy using drug loaded, block copolymer stabilized perfluorocarbon nanoemulsions. J Control Release 2011;153:4–15.
[9] Agarwal A, Huang SW, O'Donnell M, Day KC, Day M, Kotov N, et al. Targeted gold nanorod contrast agent for prostate cancer detection by photoacoustic imaging. J Appl Phys 2007;102:064701.
[10] Chen Y-S, Frey W, Kim S, Kruizinga P, Homan K, Emelianov S. Silica-coated gold nanorods as photoacoustic signal nanoamplifiers. Nano Lett 2011;11:348–54.
[11] Li P-C, Wei C-W, Liao C-K, Chen C-D, Pao K-C, Wang C-RC, et al. Photoacoustic imaging of multiple targets using gold nanorods. IEEE Trans Ultrason Ferroelectr Freq Control 2007;54:1642–7.
[12] Wilson K, Homan K, Emelianov S. Biomedical photoacoustics beyond thermal expansion using triggered nanodroplet vaporization for contrast-enhanced imaging. Nat Commun 2012;3:618.
[13] Kim K, Huang S-W, Ashkenazi S, O'Donnell M, Agarwal A, Kotov NA, et al. Photoacoustic imaging of early inflammatory response using gold nanorods. Appl Phys Lett 2007;90:223901.
[14] Wei C, Lombardo M, Larson-Smith K, Pelivanov I, Perez C, Xia J, et al. Nonlinear contrast enhancement in photoacoustic molecular imaging with gold nanosphere encapsulated nanoemulsions. Appl Phys Lett 2014;104:033701.
[15] Farny CH, Wu T, Holt RG, Murray TW, Roy RA. Nucleating cavitation from laser-illuminated nano-particles. Acoust Res Lett Online 2005;6:138–43.
[16] McLaughlan JR, Roy RA, Ju H, Murray TW. Ultrasonic enhancement of photoacoustic emissions by nanoparticle-targeted cavitation. Opt Lett 2010;35:2127–9.
[17] Ju H, Roy RA, Murray TW. Gold nanoparticle targeted photoacoustic cavitation for potential deep tissue imaging and therapy. Biomed Opt Express 2013;4:66–76.
[18] Larson-Smith K, Pozzo DC. Pickering emulsions stabilized by nanoparticle surfactants. Langmuir 2012;28:11725–32.
[19] Larson-Smith K, Pozzo DC. Scalable synthesis of self-assembling nanoparticle clusters based on controlled steric interactions. Soft Matter 2011;7:5339.
[20] Frens G. Controlled nucleation for the regulation of the particle size in monodisperse gold suspensions. Nature 1973;241:20–2.
[21] Fattaccioli J, Baudry J, Émerard J-D, Bertrand E, Goubault C, Henry N, et al. Size and fluorescence measurements of individual droplets by flow cytometry. Soft Matter 2009;5:2232.
[22] Draine BT, Flatau PJ. Discrete-dipole approximation for scattering calculations. J Opt Soc Am A 1994;11:1491.
[23] Eisenmenger W, Staudenraus J. Fibre-optic probe hydrophone for ultrasonic and shock-wave measurements in water. Ultrasonics 1993;31:267–73.
[24] Zhang P, Porter T. An in vitro study of a phase-shift nanoemulsion: a potential nucleation agent for bubble-enhanced HIFU tumor ablation. Ultrasound Med Biol 2010;36:1856–66.
[25] Sheeran PS, Luois SH, Mullin LB, Matsunaga TO, Dayton PA. Design of ultrasonically-activatable nanoparticles using low boiling point perfluorocarbons. Biomaterials 2012;33:3262–9.
[26] Kripfgans OD, Fowlkes JB, Woydt M, Eldevik OP, Carson PL. In vivo droplet vaporization for occlusion therapy and phase aberration correction. IEEE Trans Ultrason Ferroelectr Freq Control 2002;49:726–38.
[27] Schad KC, Hynynen K. In vitro characterization of perfluorocarbon droplets for focused ultrasound therapy. Phys Med Biol 2010;55:4933.
[28] Wei C, Xia J, Lombardo M, Perez C, Arnal B, Larson-Smith K, et al. Laser-induced cavitation in nanoemulsion with gold nanospheres for blood clot disruption: in vitro results. Opt Lett 2014;39:2599–602.
[29] Perez C, Brayman A, Tu J, Swalwell J, Chen H, Matula T. Acoustic and optical characterization of ultrasound contrast agents via flow cytometry. J Acoust Soc Am 2012;132:1906.
[30] Wu T, Farny CH, Roy RA, Holt RG. Modeling cavitation nucleation from laser-illuminated nanoparticles subjected to acoustic stress. J Acoust Soc Am 2011;130:3252–63.
[31] (a) Wang L, Jacques SL, Zheng L. MCML – Monte Carlo modeling of light transport in multi-layered tissues. Comput Methods Programs Biomed 1995;47:131–46; (b) Krasovitski B, Kislev H, Kimmel E. Modeling photothermal and acoustical induced microbubble generation and growth. Ultrasonics 2007;47:90–101.
[32] Sheeran PS, Wong VP, Luois S, McFarland RJ, Ross WD, Feingold S, et al. Decafluorobutane as a phase-change contrast agent for low-energy extravascular ultrasonic imaging. Ultrasound Med Biol 2011;37:1518–30.
[33] Arnal B, Wei C-W, Xia J, Pelivanov IM, Lombardo M, Perez C, et al. Inertial cavitation in theranostic nanoemulsions with simultaneous pulsed laser and low frequency ultrasound excitation, vol. 8943. 2014. 89433E–89433E–8.

Bastien Arnal received his engineering degree from Ecole Supérieure de Physique et de Chimie Industrielles de Paris (ESPCI ParisTech) in 2009 with a joint M.Sc. degree in acoustics from University Paris VII. In 2007, he worked for Phillips Research North America in Briarcliff Manor, NY, on medical ultrasonics. He received his Ph.D. at Institut Langevin in Paris. He received the Nadine Barrie Smith student award at the ISTU in 2012. He is currently a postdoc in bioengineering at the University of Washington, Seattle, USA. His research interests include medical ultrasonic imaging, ultrasonic therapy, shear wave elastography, inverse problems, time-reversal and molecular imaging using photoacoustics.

Camilo Perez is a Ph.D. student in the Bioengineering Program at the University of Washington in Seattle. He is a member of the Center for Industrial and Medical Ultrasound, working on his Ph.D. under the direction of Dr. Thomas J. Matula. He received BS degree in Electrical Engineering at the University of Delaware. His area of research involves extracorporeal shockwave therapy, ultrasound metrology characterization of shockwave fields, characterization of ultrasound contrast agents (microbubbles), and characterization of phase change emulsions as photoacoustic/ultrasound contrast agents. He is also the treasurer of the Seattle Student Chapter of the Acoustical Society of America (SSCASA).

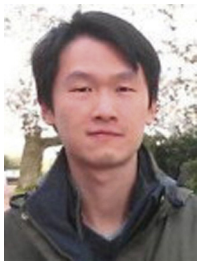

Chen-Wei Wei received the BS degree in electrical engineering from National Chiao-Tung University, Hsinchu, Taiwan, in 2003, and the MS and Ph.D. degree in electrical engineering from National Taiwan University, Taipei, Taiwan, in 2005 and 2009, respectively. He is currently a postdoctoral in bioengineering at University of Washington, Seattle, USA. His current research interests include new ultrasound and photoacoustic contrast agent and new imaging techniques.

Jinjun Xia earned his Ph.D. degree in bioengineering from University of Missouri in 2007. Currently, he is working on ultrasound and photoacoustic imaging in Dr. O'Donnell's lab at University of Washington, Seattle, WA. His research interest includes all optical methods for non-contact acoustic wave generation and detection, photoacoustic imaging, optical imaging and light-tissue interaction.

Michael Lombardo received his BS in Chemical Engineering from the University of Missouri in 2012. He then began his Ph.D. research at the University of Washington in colloidal self-assembly.

Ivan Pelivanov is an Assistant Professor at the Physics faculty of M.V. Lomonosov Moscow State University and visiting Assistant Professor at the University of Washington (WA, USA). He graduated from the group of Prof. A.A. Karabutov, which is a pioneering and renown team in various physical and biological applications of optoacoustic spectroscopy, and received his Ph.D. degree in 2000. His recent research focuses on designing sensitive wideband detectors, application of optoacoustic method in NDT & material evaluation, analytic chemistry and in medicine. He is one of the most active members in optoacoustic research for more than a decade.

Dr. Thomas J. Matula is Director of the Center for Industrial and Medical Ultrasound, and co-Director of the Ultrasound-based Center for Molecular Imaging and Therapy at the Applied Physics Laboratory, University of Washington. Dr. Matula is a Fellow of the ASA (Acoustical Society of America). His current interests include ultrasound molecular imaging and therapy, and ultrasound-based techniques for biological sample preparation and characterization.

Prof. Lilo D. Pozzo is Associate Professor of Chemical Engineering at the University of Washington in Seattle. She holds a BS in Chemical Engineering from the University of Puerto Rico Mayagüez (2001) as well as a MS Degree in Colloid, Polymers and Surfaces (2006) and a PhD in Chemical Engineering from Carnegie Mellon University (2006). She worked as a postdoctoral researcher at the NIST Center for Neutron Research and at the University of Maryland. Her research interests and expertise focus on the control and manipulation of self-assembling soft materials and their use in health, energy and engineering materials applications.

Matthew O'Donnell has worked at General Electric CRD, the University of Michigan, where he was Chair of the BME Department from 1999 to 2006, and the University of Washington (UW), where he was the Frank and Julie Jungers Dean of Engineering from 2006 to 2012. He is now Professor of Bioengineering at UW. His most recent research has focused on elasticity imaging, optoacoustic arrays, photoacoustic contrast agents, thermal strain imaging, and catheter-based devices. He is a fellow of the IEEE and AIMBE and is a member of the Washington State Academy of Sciences and the National Academy of Engineering.